

The Thermoelectric Performance of Few-Layer Transition Metal Dichalcogenides

Darshana Wickramaratne and Roger K. Lake

*Department of Electrical Engineering,
University of California, Riverside, CA 92521-0204*

Ferdows Zahid

*Department of Physics and the Center of Theoretical and Computational Physics,
The University of Hong Kong, Pokfulam Road, Hong Kong SAR, China*

Abstract

The thermoelectric figure of merit, ZT , of one to four monolayers of MoS_2 , MoSe_2 , WS_2 , and WSe_2 are calculated. Among all of the materials and layers, the maximum room temperature n-type ZT value of 2.39 occurs in bilayer MoSe_2 , and the maximum p-type ZT value of 1.15 occurs for bilayer MoS_2 . These ZT values are factors of 8 and 14, respectively, larger than the ZT values of the bulk material. The power factor and ZT change non-monotonically as the film thicknesses are increased. The peak ZT occurs in structures with thickness greater than a single monolayer. The shape of the distribution of the valence band and conduction band density of modes explains the enhanced thermoelectric performance. In all cases, the maximum ZT coincides with the sharpest turn-on of the density of modes. Effective masses, energy gaps, power-factors, and ZT values are tabulated for all materials and layer thicknesses.

I. INTRODUCTION

Semiconducting, transition-metal dichalcogenides (TMDCs) exhibit promising electronic¹⁻⁵, opto-electronic⁶ and spintronic⁷ properties. Single monolayers (three atomic layers) can be either exfoliated or grown with chemically stable surfaces. The electronic, optical, and spin properties of monolayers are qualitatively different from those of the bulk. The band gap changes from indirect to direct, and the valence band edges at the K and K' points become spin polarized.^{6,7} These materials are discussed in a number of recent reviews.⁸⁻¹²

Experimental studies conducted on a different set of two-dimensional materials, namely Bi_2Te_3 and Bi_2Se_3 , demonstrated an improvement in their thermoelectric performance as their thickness was reduced.^{13,14} A large increase in ZT has been theoretically predicted for monolayer Bi_2Te_3 compared to that of the bulk.¹⁵⁻¹⁷ This enhancement in ZT results from the unique, step-function shape of the density of modes at the valence band edge of a single quintuple layer.^{16,17} The shape of the density of modes increases the power factor, and the increase in the power factor increases ZT . For Bi_2Te_3 , the large enhancement in the power factor and in ZT only occurs for a monolayer. For bilayer and trilayer Bi_2Te_3 , the step-like shape of the density of modes disappears, and the calculated values of ZT are either slightly higher¹⁸ or slightly lower¹⁷ than that of the bulk.

Prior experimental and theoretical investigations of the thermoelectric performance of transition metal dichalcogenides have focused on either bulk or monolayer materials.^{6,19-24} There has not been a study of the effect of film thickness on the power factor and ZT in the transition metal dichalcogenides. It is not known whether the power factor and ZT are maximum at monolayer thickness or at some other thickness.

This work theoretically investigates the electronic properties and the thermoelectric performance of bulk and one to four monolayers of 4 different TMDC materials: MoS_2 , MoSe_2 , WS_2 , and WSe_2 . The goal is to understand how their thermoelectric properties vary with thickness and whether the superior thermoelectric performance predicted in a monolayer extends to thin films with a greater number of monolayers. We find that few layer n-type (p-type) TMDC materials demonstrate an improvement in ZT up to a factor of ~ 8 (~ 14) when compared to their equivalent bulk structures at room temperature. Unlike Bi_2Te_3 where the peak power factor and ZT are predicted to occur for a single monolayer, the peak

thermoelectric performance of the TMDC materials occurs at different thicknesses between one to four monolayers depending on the specific material.

Similar to monolayer Bi_2Te_3 , the increase in ZT for the ultrathin films results from an enhancement of the power factor. The increase in the power factor results from a sharper turn-on of the density of modes near the band edges. In all cases, the thickness with the more step-like density of modes has the largest value for ZT . For the semiconducting TMDCs considered here, that optimum thickness is not a single monolayer.

II. THEORETICAL METHODS

Ab-initio calculations of the bulk and few-layer structures (one to four layers) are carried out using density functional theory (DFT) with a projector augmented wave method²⁵ and the Perdew-Burke-Ernzerhof (PBE) type generalized gradient approximation^{26,27} as implemented in the Vienna *ab-initio* simulation package (VASP).^{28,29} The vdW interactions in MoSe_2 and MoS_2 are accounted for using a semi-empirical correction to the Kohn-Sham energies when optimizing the bulk structures (optimization of WS_2 and WSe_2 structures are done at the PBE level since the semi-empirical parameters for tungsten are currently not described by the dispersion potential).³⁰ The Monkhorst-Pack scheme is used for the integration of the Brillouin zone with a k-mesh of $12 \times 12 \times 6$ for the bulk structures and $12 \times 12 \times 1$ for the thin-films. The energy cutoff of the plane wave basis is 300 eV. All of the the electronic bandstructure calculations include spin-orbit coupling. Calculations are also performed without spin-orbit coupling and the results are compared.

To verify the results of the PBE calculations, the electronic structure of 1L, 2L, 3L and 4L MoS_2 are calculated using the much more computationally expensive hybrid Heyd-Scuseria-Ernzerhof (HSE) functional.³¹ The HSE calculations incorporate 25% short-range Hartree-Fock exchange. The screening parameter μ is set to 0.4 \AA^{-1} .

The thermoelectric parameters are calculated from a Landauer formalism using the *ab-initio* derived density of modes.^{16,17,23} In the linear response regime, the electronic conductivity (σ), the electronic thermal conductivity (κ_e), and the Seebeck coefficient (S) are

expressed as^{32,33}

$$\sigma = (2q^2/h)I_0 \quad (\Omega^{-1}\text{m}^{-1}), \quad (1)$$

$$\kappa_e = (2Tk_B^2/h)(I_2 - I_1^2/I_0) \quad (\text{Wm}^{-1}\text{K}^{-1}), \quad (2)$$

$$S = -(k_B/q)\frac{I_1}{I_0} \quad (\text{V/K}), \quad (3)$$

with

$$I_j = \frac{1}{L} \int_{-\infty}^{\infty} \left(\frac{E - E_F}{k_B T} \right)^j \bar{T}(E) \left(-\frac{\partial f_0}{\partial E} \right) dE \quad (4)$$

where L is the device length, q is the magnitude of the electron charge, h is Planck's constant, and k_B is Boltzmann's constant. The transmission function is

$$\bar{T}(E) = T(E)M(E) \quad (5)$$

where $M(E)$ as the density of modes (DOM). In the diffusive limit,

$$T(E) = \lambda(E)/L, \quad (6)$$

and $\lambda(E)$ is the electron mean free path. When phonon scattering is dominant, the mean free path can be written as a constant, $\lambda(E) = \lambda_0$. As discussed in Ref. [34], the transport distribution, $\Xi(E)$, arising from the Boltzmann transport equation is related to the above quantities by $\Xi(E) = \frac{2}{h}T(E)M(E)$.

The density of modes $M(E)$ can be defined as^{17,32}

$$M(E) = \left(\frac{L_{\perp}}{2\pi} \right)^{d-1} \int_{BZ} \sum_{k_{\perp}} \Theta(E - \epsilon(k_{\perp})) dk_{\perp}^{d-1} \quad (7)$$

where d is the dimensionality of the system, L_{\perp} are the dimensions of the structure perpendicular to the direction of transport ($L_{\perp}^2 = W \times t$ for $d = 3$, $L_{\perp} = W$ for $d = 2$; W = width of the structure, t = film thickness), Θ is the unit step function, and k_{\perp} refers to the k states in the first Brillouin zone perpendicular to the transport direction. Using Eq. (7), $M(E)$ of any material in any dimension can be numerically evaluated from a given electronic band structure by counting the bands that cross the energy of interest. The density of modes calculations are performed by integrating over the first Brillouin zone using a converged k point grid (51 x 51 x 10 k points for the bulk structures and 51 x 51 x 1 for the thin films).

We account for carrier scattering within each structure by fitting our theoretically calculated bulk Seebeck coefficient with bulk experimental data. An electron mean free path

of $\lambda_0 = 14$ nm gives the best agreement with experimental data on the Seebeck response of bulk MoS₂.³⁵ This value of the mean free path is also consistent with a theoretically derived energy independent phonon-limited mean free path ($\lambda_0 = 14$ nm) for electrons in monolayer MoS₂.³⁶ As an initial approximation of carrier scattering we use the same λ_0 value to model the thermoelectric properties of all the TMDC materials investigated in this study. For the lattice thermal conductivity, a κ_l value of $19.5 \text{ W m}^{-1} \text{ K}^{-1}$ obtained from a molecular dynamics simulation on MoS₂ is used.³⁷ Prior experimental³⁸ and theoretical²³ studies of the lattice thermal conductivity in the TMDC materials have demonstrated that κ_L does not vary significantly for the different TMDC compounds studied here. With the above quantities in hand, the power factor, $S^2\sigma$, and the thermoelectric figure of merit $ZT = S^2\sigma T/(\kappa_l + \kappa_e)$ are determined.

III. RESULTS

All of the thermoelectric parameters are derived from the calculated electronic bandstructures. Therefore, we begin this section with a discussion of the calculated bandstructures. The bandstructure calculations produce considerably more information than is required for calculating the thermoelectric parameters. To preserve that information and contribute towards a database of material parameters, extracted properties such as effective masses and energy gaps at high symmetry points are tabulated.

Figure 1 shows the *ab-initio* band structure of one-layer (1L) through four-layer (4L) and bulk WS₂. The large valence band splitting at the *K*-point and the direct-indirect gap transition as the film thickness increases above 1L are features that occur in the other TMDC materials included as part of this study. The last panel in Fig. 1 illustrates the effect of decreasing layer thickness on the bandgap for all of the materials studied. The optimized lattice parameters of the bulk TMDC compounds are listed in Table I. The results in Table I and Figure 1 are consistent with prior experimental characterization^{39–41} and theoretical calculations of the bulk^{42,43} and thin film^{44,45} crystal structures and electronic band structures. The results of these electronic structure calculations at the high symmetry points are summarized in Tables II and Table III. Table II gives the relative effective masses, and Table III gives the energy gaps.

A number of prior theoretical studies of the electronic structure of monolayer and few-

layer TMDCs did not include spin-orbit interaction.^{46–48} As a result, the band bandgaps reported in those studies are slightly larger. For example the bandgaps reported in a prior PBE level calculation⁴⁸ are greater by 70 meV, 260 meV and 284 meV for MoS₂ and MoSe₂, WS₂ and WSe₂ respectively when compared to our calculation results. Without the inclusion of spin-orbit interaction, our values for the bandgap of the monolayer TMDCs are consistent with the bandgaps reported in these studies. Including spin-orbit coupling results in a splitting of the valence bands, Δ_{SO} , at K . The spin orbit interaction shifts up one of the degenerate valence bands, and this reduces the bandgap. The degree of the energy shift ranges from 39.6 meV for MoS₂ to 210.9 meV for WS₂. The second degenerate valence band is shifted down by an energy that is also unique to each TMDC material; this ranges from 110.4 meV for MoS₂ to 316.2 meV for WSe₂. For example the calculated Δ_{SO} energies of the monolayer TMDCs are 150 meV, 181 meV, 425 meV and 461 meV for MoS₂, MoSe₂, WS₂ and WSe₂, respectively. This is in good agreement with a prior PBE level calculation⁴⁹ that accounted for spin-orbit interaction which obtained Δ_{SO} values of 146 meV, 183 meV, 425 meV and 461 meV for MoS₂, MoSe₂, WS₂ and WSe₂, respectively, and a Δ_{SO} energy of 188 meV obtained for monolayer MoS₂ with the use of optical absorption experiments.⁵⁰

More sophisticated many-body *ab-initio* calculations which include HSE or GW calculations have been reported in prior studies of the band structure of monolayer^{49,51–53} and bilayer^{51,53} structures of the molybdenum and tungsten dichalcogenides. The values for Δ_{SO} resulting from these theories are only slightly changed from those of the PBE model. The Δ_{SO} values reported for monolayer MoS₂, MoSe₂, WS₂ and WSe₂ with a GW (HSE) calculation are 164 (193) meV, 212 (261) meV, 456 (521) meV and 501 (586) meV.⁴⁹ The primary difference between the PBE and the HSE and GW calculations is an increase in the bandgap. However, the PBE bandgap is large enough compared to the temperatures considered that the exact magnitude of the bandgap has no effect on the thermoelectric parameters. An explicit comparison of the electronic structure and the thermoelectric parameters calculated from the PBE and the HSE functionals for 1L - 4L MoS₂ is given below.

Calculation of the thermoelectric parameters requires the density of modes extracted from the electronic bandstructure using Eq. (7). Figure 2 shows the density of modes versus energy for bulk, 1L, 2L, 3L, and 4L MoS₂, MoSe₂, WS₂, and WSe₂. To compare the density of modes of the bulk structure with the thin-film structures, we divide the density of modes of the thin-film structures by their respective thickness, t . As will be shown, for

these TMDCs, small variations in the shape of the density of modes near the band edges can enhance the power factor and subsequently ZT. The thermoelectric properties of the bulk and thin-film structures are calculated from Eqs. (1) - (6) using the density of modes shown in Fig. 2.

The Seebeck coefficient, power-factor (PF), and the thermoelectric figure-of-merit (ZT) as a function of the reduced Fermi level, η_F are shown in Figures 3, 4, and 5, respectively. The reduced Fermi-level is $\eta_F = \frac{E_F - E_{C1}}{kT}$ for electrons in the conduction band, and $\eta_F = \frac{E_F - E_{V1}}{kT}$ for holes in the valence band. E_{C1} and E_{V1} are the energies of the conduction and valence band edges, respectively. For each material and each thickness the maximum power factor and ZT occurs for the conduction band states. The peak conduction band and valence band power factor and ZT for each structure and material at 77K, 150K and 300K are summarized in Table IV and Table V, respectively. For all materials, the few layer structures show a large increase in the values of their power factor and ZT compared to those of the bulk.

The peak n-type ZT values (and corresponding layer thicknesses) for MoS₂, MoSe₂, WS₂ and WSe₂ are 2.23 (t=3L), 2.39 (t=2L), 2.03 (t=3L) and 1.91 (t=2L) which is an improvement by a factor of 6.4, 8.2, 7.2 and 7.5 over the respective bulk values. These peak ZT values occur when the Fermi level is moved by 1.393kT, 1.547kT, 1.083kT and 1.393kT, respectively, below the conduction band at T=300K. The peak p-type ZT values (and corresponding layer thicknesses) for MoS₂, MoSe₂, WS₂ and WSe₂ are 1.15 (t=2L), 0.81 (t=2L-4L), 0.76 (t=2L-3L) and 0.62 (t=1L-4L) which is an improvement by a factor of 14.4, 10.1, 9.5 and 5.2 over the respective bulk values. These peak ZT values occur when the Fermi level is moved by 1.16kT, 1.006kT, 0.928kT and 0.851kT, respectively, above the valence band at T=300K. Of the four TMDC materials studied, MoS₂ is the only material to exhibit a p-type and n-type ZT > 1. In contrast to Bi₂Te₃, the peak value of ZT does not occur in any of the materials for the monolayer thickness.

The Seebeck coefficients at the maximum n-type (p-type) ZT for each material are 275 (245.6) μVK^{-1} , 287 (230.7) μVK^{-1} , 279 (230.1) μVK^{-1} and 276 (216.7) μVK^{-1} for MoS₂, MoSe₂, WS₂ and WSe₂ respectively. However, the Seebeck coefficients at the maximum n-type (p-type) power factor for each material are 167 (90.4) μVK^{-1} , 100 (185.8) μVK^{-1} , 165 (177.1) μVK^{-1} and 171 (172.1) μVK^{-1} for MoS₂, MoSe₂, WS₂ and WSe₂ respectively; which is generally consistent with the conclusion of a report on engineering the Seebeck coefficient to obtain the maximum thermoelectric power factor.⁵⁴

Without the inclusion of spin-orbit interaction our values of the ballistic ZT for the monolayer TMDC materials are consistent with a prior report on the monolayer thermoelectric properties of these TMDC materials.²³ Our calculations show that without the inclusion of spin-orbit interaction the peak n-type ZT values for all materials continue to occur at thicknesses above a single monolayer. The peak n-type ZT values (and corresponding layer thicknesses) without spin-orbit interaction for MoS₂, MoSe₂, WS₂ and WSe₂ are 1.3779 (t=3L), 1.5222 (t=2L), 1.1278 (t=4L) and 1.2812 (t=2L). However, the peak p-type ZT values without spin-orbit interaction occurs for a single monolayer for each TMDC material. The p-type ZT values without spin-orbit interaction for MoS₂, MoSe₂, WS₂ and WSe₂ are 1.4157, 0.8368, 0.8972 and 0.6898.

Recent electronic structure calculations using the Heyd-Scuseria-Ernzerhof (HSE) hybrid functional⁵⁵ give a bandgap that more accurately matches known experimental values.⁵⁵ To assess whether the trends in the thermoelectric parameters predicted with the PBE functional are the same as those resulting from the HSE functional, we calculate the electronic band structure of 1L, 2L, 3L and 4L MoS₂ with both the PBE and the HSE functional and plot the results in Fig. 6. Near the band edges, the HSE energies appear to be shifted with respect to the PBE energies. The effective masses for the HSE band structures are lower by up to 17% for the conduction band valleys at K and Σ and are lower by up to 11% for the valence band valleys at K and Γ .

To verify that the HSE functional leaves the thermoelectric trends predicted from the PBE functional unchanged, we compute the density-of-modes and thermoelectric performance of 1L, 2L and 3L MoS₂ using the HSE functional with the inclusion of spin orbit coupling. Figure 7 illustrates the DOM, Seebeck coefficient, power factor and ZT for the 1L, 2L and 3L structures of MoS₂ computed with the HSE functional. The quantitative values do differ. For the MoS₂ trilayer structure, the HSE (PBE) functionals give a peak n-type power factor of 0.41 (0.28) WK⁻²m⁻² and a peak n-type ZT of 2.4 (2.2). However, the HSE results for few-layer MoS₂ structures demonstrate the same trends in the shape of the density of modes and the same trends in the values for the power factors and ZT. Both the HSE and PBE calculations show that the turn-on of the density of modes is sharpest for the tri-layer structure resulting in maximum values for the power factor and ZT. Since the primary effect on the low energy states of the exact exchange in the HSE functional is to shift the band edges with respect to those of a PBE calculation, the trends resulting from the shape of the

density of modes should be preserved.

Figure 8 summarizes the values from the PBE calculations for the peak n-type and p-type ZT and power factors for each TMDC material and layer thickness. In the n-type MoSe₂, WS₂ and WSe₂ structures, the peak power-factor and the peak ZT do not occur at the same film thickness. For example, in MoSe₂, a single monolayer has the highest power factor, and a bilayer has the highest ZT. This can be explained by the increase in the electronic thermal conductivity, κ_e as the Fermi level is moved into the conduction band.

Figure 9 shows the ratio of the total thermal conductivity, κ_{tot} , with respect to the lattice thermal conductivity, κ_l , for each TMDC material. The two guide lines on each figure illustrate the reduced Fermi level position at which the maximum n-type power factor and ZT occurs. The ratio $\kappa_{\text{tot}}/\kappa_l = 1 + \kappa_e/\kappa_l$ is higher at the Fermi level position where the maximum power factor occurs. This increase in κ_e explains why the peak power factor and ZT occur at different Fermi energies and film thicknesses.

The thermoelectric performance in the low dimensional structures is enhanced by the more abrupt step-like shape of the density of modes distribution.³⁴ The conduction band DOM distribution for the maximum and minimum ZT structures for each material are plotted in Figure 10. In all cases, the DOM with the sharper turn-on at the band edge gives rise the the maximum value for ZT.

To further analyze the effect of the density of modes step-like shape on the thermoelectric performance, we consider a model shape function for a single mode in which the smoothness of the turn-on can be continually adjusted.

$$DOM_{\text{step}}(E) = 1 - f(E/\sigma) \quad (8)$$

In Eq. (8), $f(E/\sigma)$ is the Fermi-Dirac function, σ determines the ‘sharpness’ of the turn-on of the step function, and E is energy. The ballistic power factor with $T(E) = 1$ is numerically evaluated for different values of σ . Figure 11 illustrates the density of mode step functions and the numerically evaluated power factors as a function of the Fermi level position for three values of σ at room temperature: 0, $k_B T$, and $10k_B T$. As the DOM evolves from a Heaviside step function to smoother transitions, the power factor decreases by a factor of 1.8. It is clear from Eq. (4), that with $E_F \leq 0$, a step-function density of modes removes all negative contributions to the integrand of I_1 giving a maximum value for I_1 . Thus, these semi-analytical results support the numerically observed trends that the density of modes

with the sharpest turn-on gives rise to the largest power factor and ZT.

IV. SUMMARY

The electronic structure of one to four monolayers of the semiconducting transition metal dichalcogenides MoS₂, MoSe₂, WS₂ WSe₂ are calculated using DFT with spin-orbit coupling and the PBE functional. Comparisons are made to results in the absence of spin-orbit coupling, and the PBE results are compared to HSE calculations for MoS₂. The peak n-type value of ZT increases by a factor of 6–8 over the bulk value for all materials. Among the 4 materials and 4 thicknesses, bilayer MoSe₂ gives the maximum n-type ZT value of 2.4. The peak p-type value of ZT increases by a factor of 5 – 14 over the bulk value for all materials. The maximum p-type ZT value of 1.2 occurs for bilayer MoS₂. The maximum value of ZT occurs at layer thicknesses greater than one monolayer for all materials. The maximum power factor generally occurs for a different layer thickness and at a more degenerate Fermi level than the maximum value of ZT. This difference can be explained by the increased electrical thermal conductivity at the Fermi level of the maximum power factor. For all materials, the maximum value of ZT coincides with the sharpest turn-on of the density of modes distribution at the band edge.

Acknowledgments

This work is supported in part by the National Science Foundation (NSF) Grant Nos. 1124733 and 1128304 and the Semiconductor Research Corporation (SRC) Nanoelectronic Research Initiative as a part of the Nanoelectronics for 2020 and Beyond (NEB-2020) program, FAME, one of six centers of STARnet, a Semiconductor Research Corporation program sponsored by MARCO and DARPA, and the University Grant Council (Contract No. AoE/P-04/08) of the Government of HKSA (FZ). This work used the Extreme Science and Engineering Discovery Environment (XSEDE), which is supported by National Science Foundation grant number OCI-1053575.

-
- ¹ B. Radisavljevic, A. Radenovic, J. Brivio, V. Giacometti, and A. Kis, *Nature Nanotechnology* **6**, 147 (2011), URL <http://www.nature.com/nnano/journal/v6/n3/abs/nnano.2010.279.html>.
 - ² Y. Yoon, K. Ganapathi, and S. Salahuddin, *Nano Letters* **11**, 3768 (2011), <http://pubs.acs.org/doi/pdf/10.1021/nl2018178>, URL <http://pubs.acs.org/doi/abs/10.1021/nl2018178>.
 - ³ H. Fang, S. Chuang, T. C. Chang, K. Takei, T. Takahashi, and A. Javey, *Nano Letters* **12**, 3788 (2012).
 - ⁴ K. Alam and R. K. Lake, *IEEE Trans. Electron Devices* **59**, 3250 (2012).
 - ⁵ A. N. Han Liu and P. Ye, *ACS Nano* **6**, 8563 (2012).
 - ⁶ T. Li and G. Galli, *The Journal of Physical Chemistry C* **111**, 16192 (2007), <http://pubs.acs.org/doi/pdf/10.1021/jp075424v>, URL <http://pubs.acs.org/doi/abs/10.1021/jp075424v>.
 - ⁷ D. Xiao, G.-B. Liu, W. Feng, X. Xu, and W. Yao, *Phys. Rev. Lett.* **108**, 196802 (2012), URL <http://link.aps.org/doi/10.1103/PhysRevLett.108.196802>.
 - ⁸ K. S. Novoselov and A. H. C. Neto, *Physica Scripta* **2012**, 014006 (2012), URL <http://stacks.iop.org/1402-4896/2012/i=T146/a=014006>.
 - ⁹ Q. H. Wang, K. Kalantar-Zadeh, A. Kis, J. N. Coleman, and M. S. Strano, *Nature Nanotech.* **7**, 699 (2012).
 - ¹⁰ A. Geim and I. Grigorieva, *Nature* **499**, 419 (2013), URL <http://www.nature.com/nature/journal/v499/n7459/abs/nature12385.html>.
 - ¹¹ M. Xu, T. Liang, M. Shi, and H. Chen, *Chemical Reviews* **113**, 3766 (2013), <http://pubs.acs.org/doi/pdf/10.1021/cr300263a>, URL <http://pubs.acs.org/doi/abs/10.1021/cr300263a>.
 - ¹² S. Z. Butler, S. M. Hollen, L. Cao, Y. Cui, J. A. Gupta, H. R. Gutierrez, T. F. Heinz, S. S. Hong, J. Huang, A. F. Ismach, et al., *ACS Nano* **7**, 2898 (2013), <http://pubs.acs.org/doi/pdf/10.1021/nn400280c>, URL <http://pubs.acs.org/doi/abs/10.1021/nn400280c>.
 - ¹³ Y. Sun, H. Cheng, S. Gao, Q. Liu, Z. Sun, C. Xiao, C. Wu,

- S. Wei, and Y. Xie, Journal of the American Chemical Society **134**, 20294 (2012), <http://pubs.acs.org/doi/pdf/10.1021/ja3102049>, URL <http://pubs.acs.org/doi/abs/10.1021/ja3102049>.
- ¹⁴ V. Goyal, D. Teweldebrhan, and A. A. Balandin, Applied Physics Letters **97**, 133117 (pages 3) (2010), URL <http://link.aip.org/link/?APL/97/133117/1>.
- ¹⁵ P. Ghaemi, R. S. K. Mong, and J. E. Moore, Phys. Rev. Lett. **105**, 166603 (2010), URL <http://link.aps.org/doi/10.1103/PhysRevLett.105.166603>.
- ¹⁶ F. Zahid and R. Lake, Applied Physics Letters **97**, 212102 (pages 3) (2010), URL <http://link.aip.org/link/?APL/97/212102/1>.
- ¹⁷ J. Maassen and M. Lundstrom, Applied Physics Letters **102**, 093103 (pages 4) (2013), URL <http://link.aip.org/link/?APL/102/093103/1>.
- ¹⁸ F. Zahid and R. K. Lake, Unpublished.
- ¹⁹ A. Amara, Y. Frongillo, M. J. Aubin, S. Jandl, J. M. Lopez-Castillo, and J. P. Jay-Gerin, Phys. Rev. B **36**, 6415 (1987), URL <http://link.aps.org/doi/10.1103/PhysRevB.36.6415>.
- ²⁰ H. Imai, Y. Shimakawa, and Y. Kubo, Phys. Rev. B **64**, 241104 (2001), URL <http://link.aps.org/doi/10.1103/PhysRevB.64.241104>.
- ²¹ H. Guo, T. Yang, P. Tao, Y. Wang, and Z. Zhang, Journal of Applied Physics **113**, 013709 (pages 7) (2013), URL <http://link.aip.org/link/?JAP/113/013709/1>.
- ²² M. Buscema, M. Barkelid, V. Zwiller, H. S. J. van der Zant, G. A. Steele, and A. Castellanos-Gomez, Nano Letters **0**, null (0), <http://pubs.acs.org/doi/pdf/10.1021/nl303321g>, URL <http://pubs.acs.org/doi/abs/10.1021/nl303321g>.
- ²³ W. Huang, H. Da, and G. Liang, Journal of Applied Physics **113**, 104304 (pages 7) (2013), URL <http://link.aip.org/link/?JAP/113/104304/1>.
- ²⁴ C. Lee, J. Hong, M.-H. Whangbo, and J. H. Shim, Chemistry of Materials **25**, 3745 (2013), <http://pubs.acs.org/doi/pdf/10.1021/cm402281n>, URL <http://pubs.acs.org/doi/abs/10.1021/cm402281n>.
- ²⁵ P. E. Blöchl, Phys. Rev. B **50**, 17953 (1994).
- ²⁶ J. P. Perdew, K. Burke, and M. Ernzerhof, Phys. Rev. Lett. **77**, 3865 (1996).
- ²⁷ M. Ernzerhof and G. E. Scuseria, J. Chem. Phys. **110**, 5029 (1999).
- ²⁸ G. Kresse and J. Hafner, Phys. Rev. B **48**, 13115 (1993).
- ²⁹ G. Kresse and J. Furthmüller, Comput. Mater. Sci. **6**, 15 (1996).

- ³⁰ S. Grimme, *Journal of Computational Chemistry* **27**, 1787 (2006), ISSN 1096-987X, URL <http://dx.doi.org/10.1002/jcc.20495>.
- ³¹ J. Heyd, G. E. Scuseria, and M. Ernzerhof, *The Journal of Chemical Physics* **118**, 8207 (2003), URL <http://scitation.aip.org/content/aip/journal/jcp/118/18/10.1063/1.1564060>.
- ³² C. Jeong, R. Kim, M. Luisier, S. Datta, and M. Lundstrom, *Journal of Applied Physics* **107**, 023707 (pages 7) (2010), URL <http://link.aip.org/link/?JAP/107/023707/1>.
- ³³ A. Paul, S. Salamat, C. Jeong, G. Klimeck, and M. Lundstrom, *Journal of Computational Electronics* **11**, 56 (2012), ISSN 1569-8025, URL <http://dx.doi.org/10.1007/s10825-011-0379-2>.
- ³⁴ R. Kim, S. Datta, and M. S. Lundstrom, *Journal of Applied Physics* **105**, 034506 (pages 6) (2009), URL <http://link.aip.org/link/?JAP/105/034506/1>.
- ³⁵ R. Mansfield and S. A. Salam, *Proceedings of the Physical Society. Section B* **66**, 377 (1953), URL <http://stacks.iop.org/0370-1301/66/i=5/a=305>.
- ³⁶ K. Kaasbjerg, K. S. Thygesen, and K. W. Jacobsen, *Phys. Rev. B* **85**, 115317 (2012), URL <http://link.aps.org/doi/10.1103/PhysRevB.85.115317>.
- ³⁷ V. Varshney, S. S. Patnaik, C. Muratore, A. K. Roy, A. A. Voevodin, and B. L. Farmer, *Computational Materials Science* **48**, 101 (2010), ISSN 0927-0256, URL <http://www.sciencedirect.com/science/article/pii/S0927025609004583>.
- ³⁸ C. Chiritescu, D. G. Cahill, N. Nguyen, D. Johnson, A. Bodapati, P. Keblinski, and P. Zschack, *Science* **315**, 351 (2007).
- ³⁹ K. Bronsema, J. De Boer, and F. Jellinek, *Zeitschrift fur anorganische und allgemeine Chemie* **540**, 15 (2004).
- ⁴⁰ W. Schutte, J. D. Boer, and F. Jellinek, *Journal of Solid State Chemistry* **70**, 207 (1987), URL <http://www.sciencedirect.com/science/article/pii/0022459687900570>.
- ⁴¹ K. K. Kam and B. A. Parkinson, *The Journal of Physical Chemistry* **86**, 463 (1982), <http://pubs.acs.org/doi/pdf/10.1021/j100393a010>, URL <http://pubs.acs.org/doi/abs/10.1021/j100393a010>.
- ⁴² H. Jiang, *The Journal of Physical Chemistry C* **116**, 7664 (2012), <http://pubs.acs.org/doi/pdf/10.1021/jp300079d>, URL <http://pubs.acs.org/doi/abs/10.1021/jp300079d>.
- ⁴³ R. Coehoorn, C. Haas, J. Dijkstra, C. J. F. Flipse, R. A. de Groot, and A. Wold, *Phys. Rev. B*

- 35**, 6195 (1987), URL <http://link.aps.org/doi/10.1103/PhysRevB.35.6195>.
- ⁴⁴ Y. Ding, Y. Wang, J. Ni, L. Shi, S. Shi, and W. Tang, *Physica B: Condensed Matter* **406**, 2254 (2011), ISSN 0921-4526, URL <http://www.sciencedirect.com/science/article/pii/S0921452611002651>.
- ⁴⁵ A. Kuc, N. Zibouche, and T. Heine, *Phys. Rev. B* **83**, 245213 (2011), URL <http://link.aps.org/doi/10.1103/PhysRevB.83.245213>.
- ⁴⁶ L. Liu, S. Bala Kumar, Y. Ouyang, and J. Guo, *Electron Devices, IEEE Transactions on* **58**, 3042 (2011), ISSN 0018-9383.
- ⁴⁷ A. Kuc, N. Zibouche, and T. Heine, *Phys. Rev. B* **83**, 245213 (2011).
- ⁴⁸ Y. Ding, Y. Wang, J. Ni, L. Shi, S. Shi, and W. Tang, *Physica B: Condensed Matter* **406**, 2254 (2011), URL <http://www.sciencedirect.com/science/article/pii/S0921452611002651>.
- ⁴⁹ A. Ramasubramaniam, *Phys. Rev. B* **86**, 115409 (2012), URL <http://link.aps.org/doi/10.1103/PhysRevB.86.115409>.
- ⁵⁰ K. F. Mak, C. Lee, J. Hone, J. Shan, and T. F. Heinz, *Phys. Rev. Lett.* **105**, 136805 (2010), URL <http://link.aps.org/doi/10.1103/PhysRevLett.105.136805>.
- ⁵¹ T. Cheiwchanchamngij and W. R. Lambrecht, *Phys. Rev. B* **85**, 205302 (2012), URL <http://link.aps.org/doi/10.1103/PhysRevB.85.205302>.
- ⁵² H. Shi, H. Pan, Y.-W. Zhang, and B. I. Yakobson, *Phys. Rev. B* **87**, 155304 (2013), URL <http://link.aps.org/doi/10.1103/PhysRevB.87.155304>.
- ⁵³ F. Zahid, L. Liu, Y. Zhu, J. Wang, and H. Guo, *AIP Advances* **3**, 052111 (pages 6) (2013), URL <http://link.aip.org/link/?ADV/3/052111/1>.
- ⁵⁴ P. Pichanusakorn and P. R. Bandaru, *Applied Physics Letters* **94**, (2009), URL <http://scitation.aip.org/content/aip/journal/apl/94/22/10.1063/1.3147186>.
- ⁵⁵ F. Zahid, L. Liu, Y. Zhu, J. Wang, and H. Guo, *AIP Advances* **3**, 052111 (pages 6) (2013), URL <http://link.aip.org/link/?ADV/3/052111/1>.
- ⁵⁶ H. Zeng, G.-B. Liu, J. Dai, Y. Yan, B. Zhu, R. He, L. Xu, S. Xu, X. Chen, and X. Cui, *Nature Scientific Reports* **3** (2013).

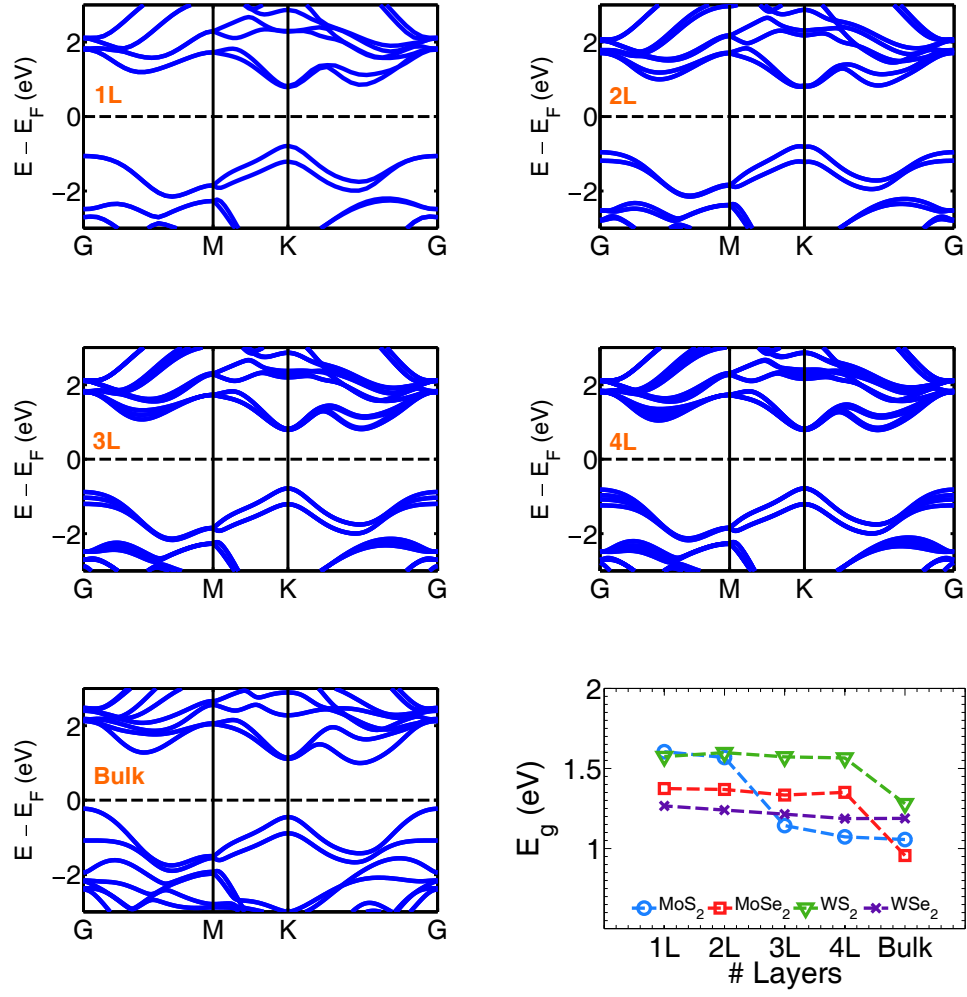


FIG. 1: *Ab-initio* calculated band structures of WS₂: 1L, 2L, 3L, 4L and bulk. The bottom right panel illustrates the variation of the band gap of the TMDC materials as a function of the number of layers.

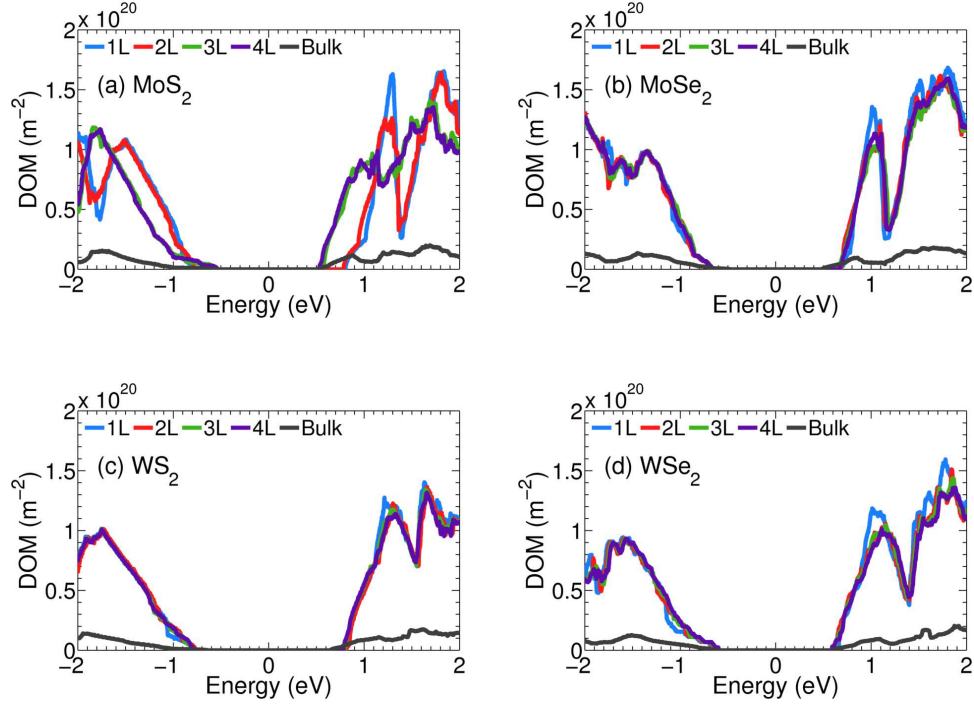


FIG. 2: (Color online) Distribution of modes per unit area versus energy for (a) MoS_2 , (b) MoSe_2 , (c) WS_2 and (d) WSe_2 for bulk (black), 1L (blue), 2L (red), 3L (green) and 4L (purple) structures. The midgap energy is set to $E=0$.

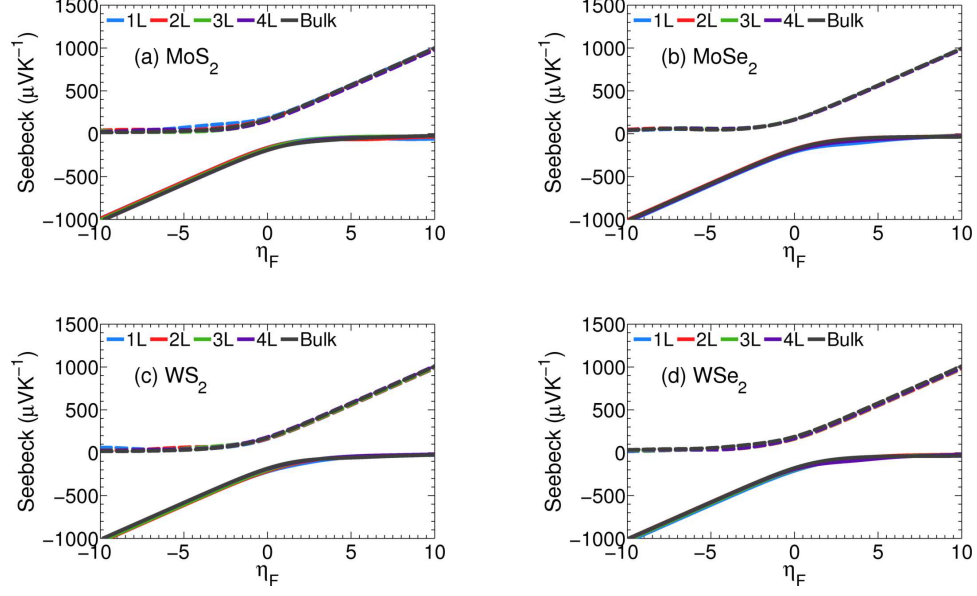


FIG. 3: (Color online) Seebeck coefficient at 300K for (a) MoS₂, (b) MoSe₂, (c) WS₂ and (d) WSe₂ for bulk (black), 1L (blue), 2L (red), 3L (green) and 4L (purple) structures. The n-type Seebeck coefficients are plotted with a solid line and p-type coefficients with a broken line as a function of the reduced Fermi energy, η_F .

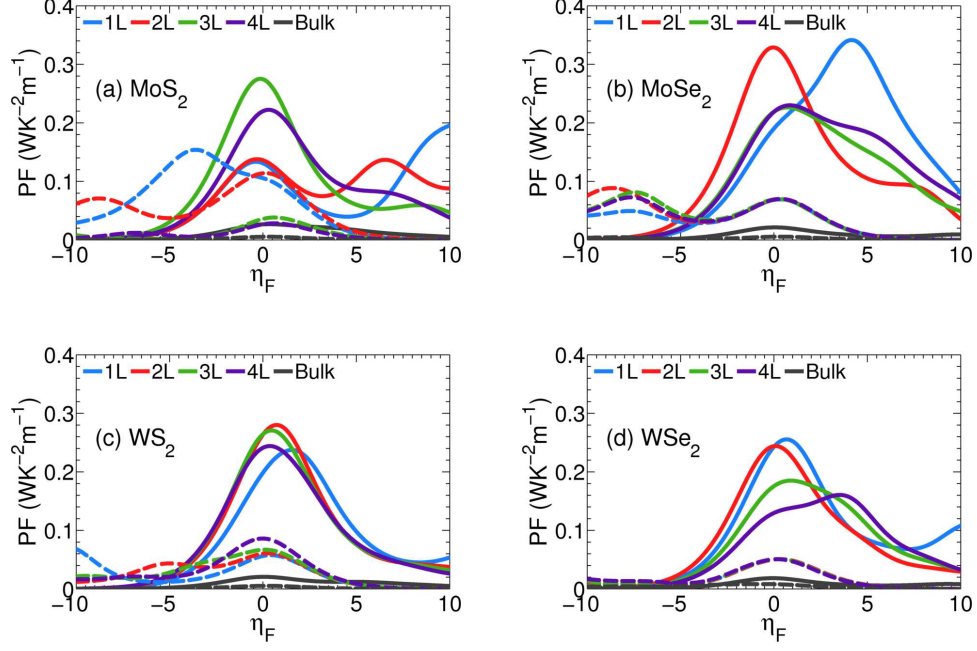


FIG. 4: (Color online) Power factor (PF) at 300K for (a) MoS_2 , (b) MoSe_2 , (c) WS_2 and (d) WSe_2 for bulk (black), 1L (blue), 2L (red), 3L (green) and 4L (purple) structures. The n-type power factors are plotted with a solid line and p-type PFs with a broken line as a function of the reduced Fermi energy, η_F .

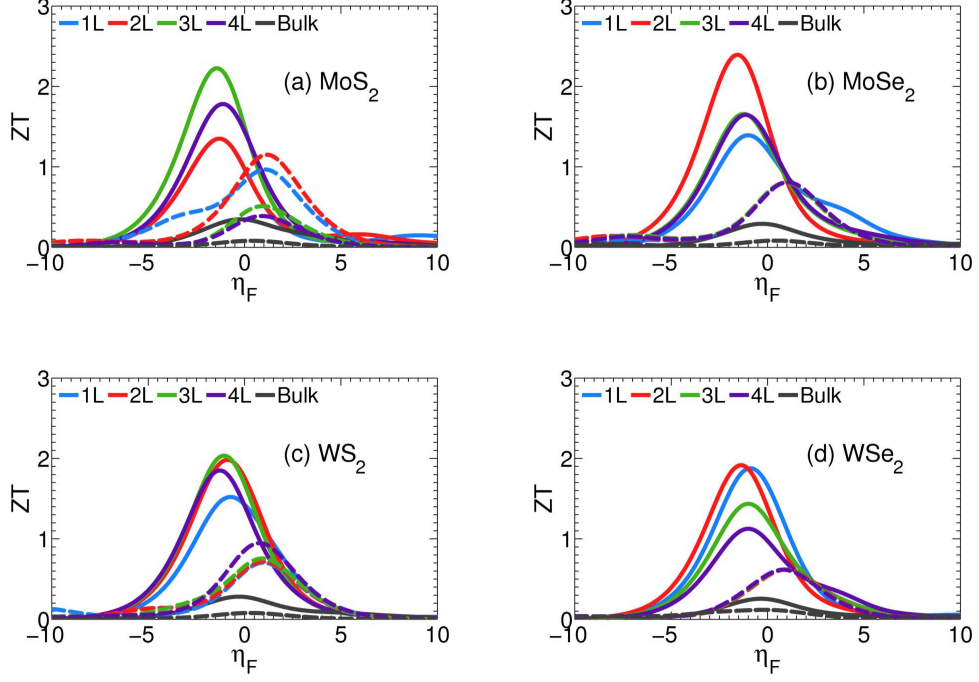


FIG. 5: (Color online) ZT at 300K for (a) MoS_2 , (b) MoSe_2 , (c) WS_2 and (d) WSe_2 for bulk (black), 1L (blue), 2L (red), 3L (green) and 4L (purple) structures. The n-type ZT is plotted with a solid line and p-type ZT with a broken line as a function of the reduced Fermi energy, η_F .

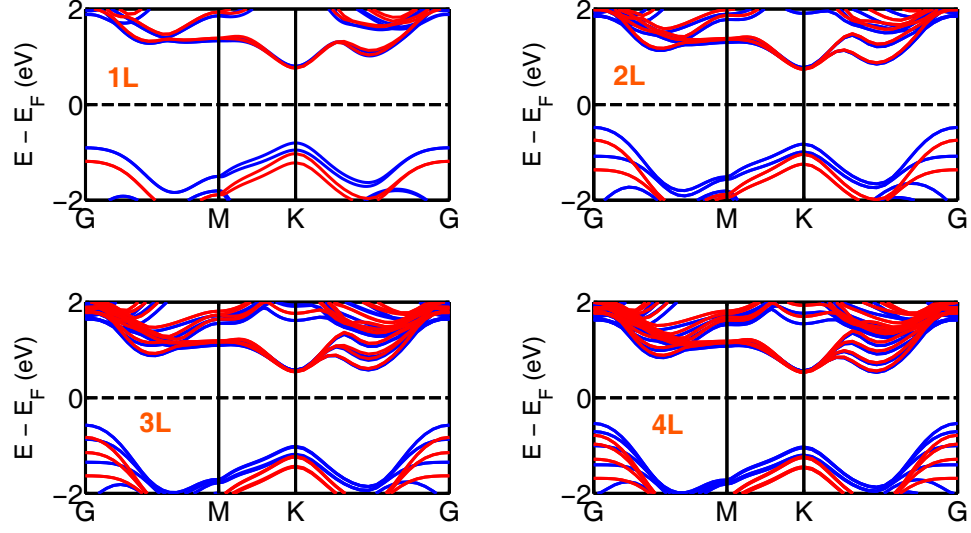


FIG. 6: *Ab-initio* calculated electronic structure of MoS₂: 1L, 2L, 3L and 4L structures using a PBE (blue) and hybrid HSE (red) functional. The HSE functional provides a correction to the underestimated PBE bandgap while the salient features of the electronic structure that would affect the density-of-modes calculation remain the same.

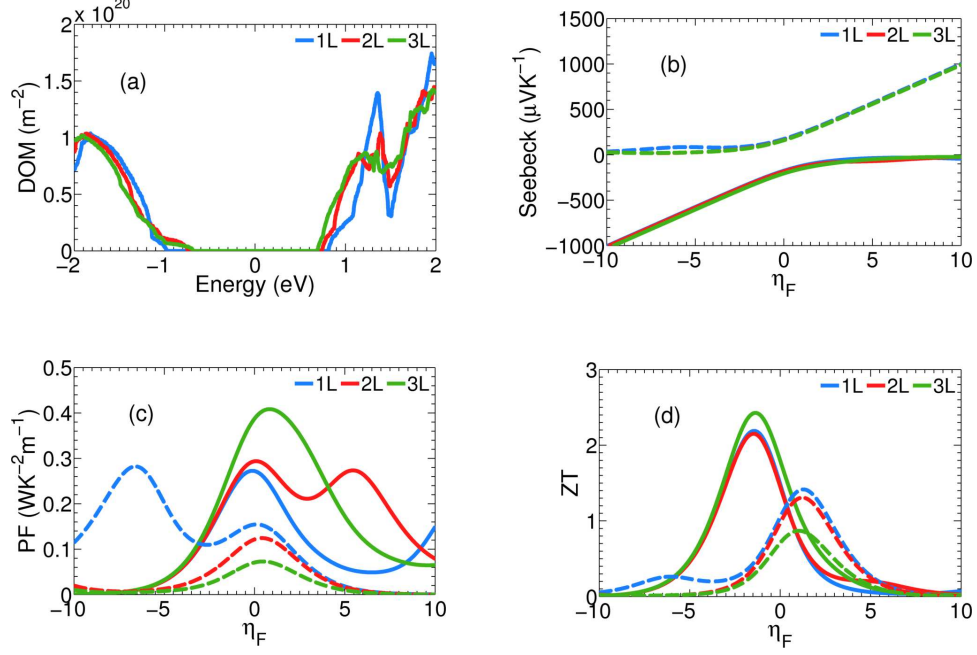


FIG. 7: (Color online) HSE calculation of the (a) density-of-modes, (b) Seebeck coefficient, (c) Power factor and (d) ZT 1L (blue), 2L (red), 3L (green) MoS₂. The n-type thermoelectric parameters are plotted with a solid line and the p-type parameters are plotted with a broken line as a function of the reduced Fermi energy, η_F .

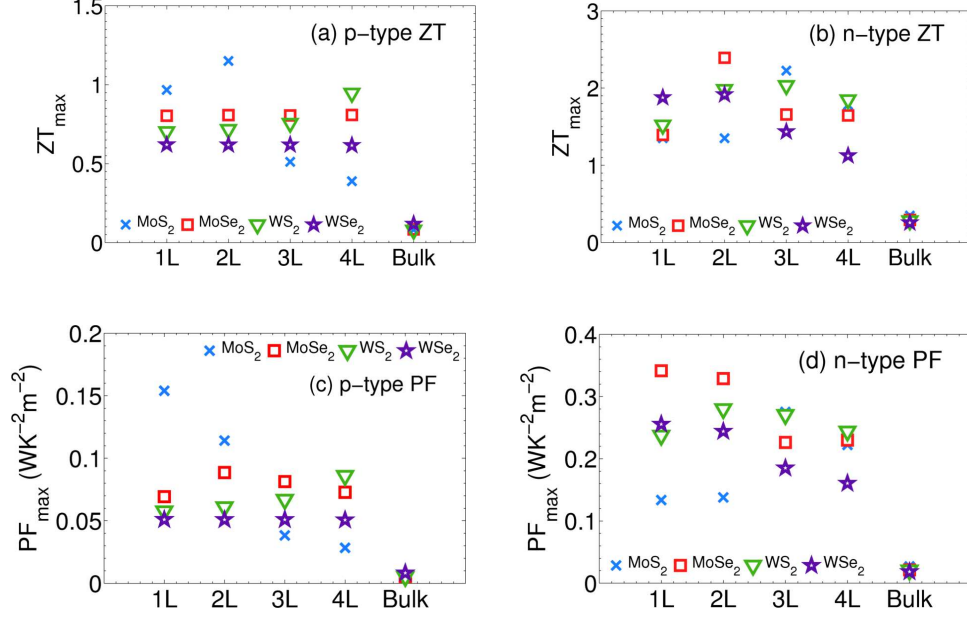


FIG. 8: (Color online) Maximum thermoelectric performance for 1 (blue), 2L (red), 3L (green), 4L (purple) and bulk (black) MoS₂, MoSe₂, WS₂, WSe₂ at 300K: (a) Maximum p-type ZT, (b) Maximum n-type ZT, (c) Maximum p-type power factor, (d) Maximum n-type power factor.

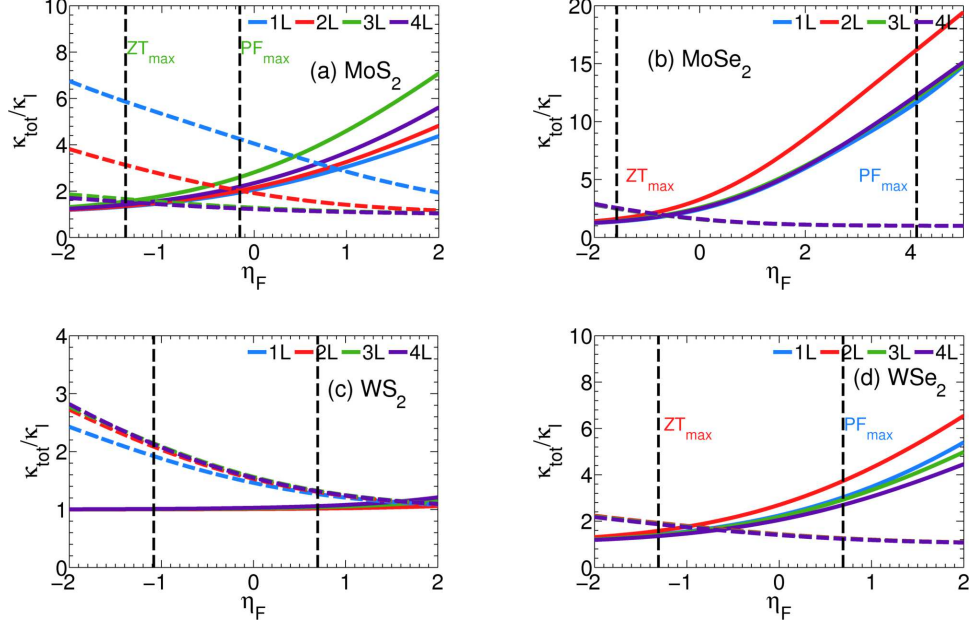


FIG. 9: (Color online) Ratio of total thermal conductivity ($\kappa_l + \kappa_e$) over the lattice thermal conductivity (κ_l) at 300K for (a) MoS₂, (b) MoSe₂, (c) WS₂, (d) WSe₂ for 1L (blue), 2L (red), 3L (green) and 4L (purple) structures. The n-type ratio is plotted with a solid line and p-type ratio with a broken line as a function of the reduced Fermi energy, η_F .

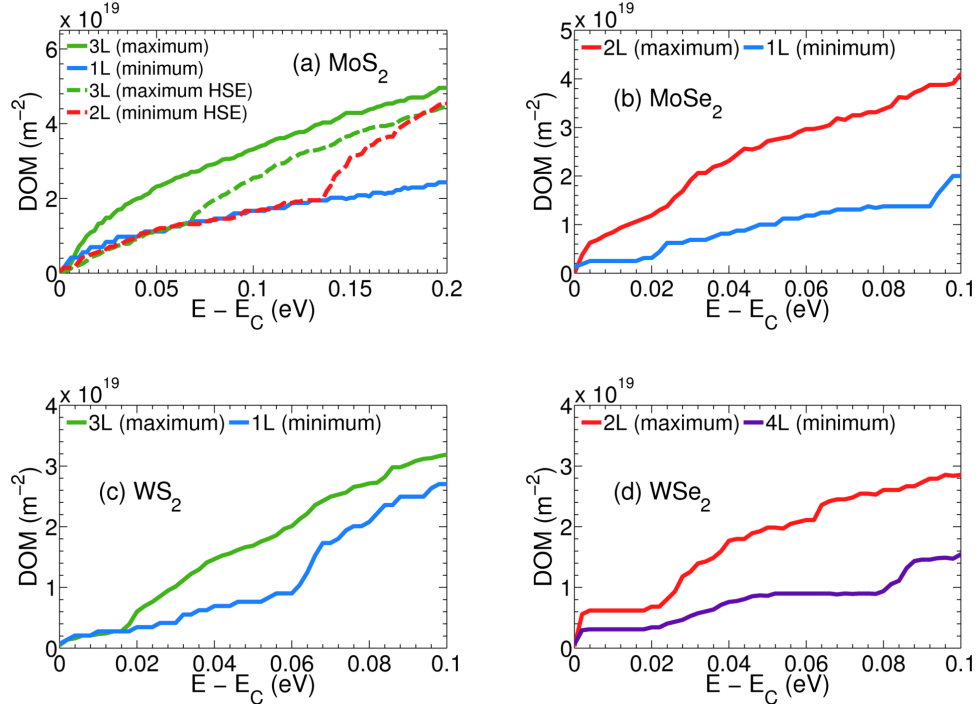


FIG. 10: (Color online) Conduction band density of modes (DOM) for (a) MoS₂, (b) MoSe₂, (c) WS₂ and (d) WSe₂ at film thicknesses where the maximum and the minimum ZT occurs with respect to the energy away from the conduction band edge, E_C .

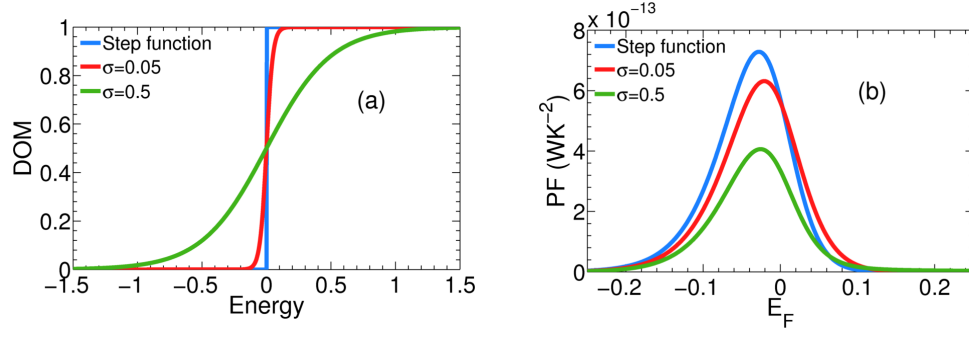


FIG. 11: (Color online) (a) Step function density of modes of a single mode for different degrees of 'smoothness' determined by the parameter σ with values of σ equal to 0, $k_B T$, and $10k_B T$ and $T=300\text{K}$. (b) Power factor for each step function density of modes distribution as a function of the Fermi level.

	$a_0(\text{\AA})$	$c_0(\text{\AA})$	z	$a_0^{expt}(\text{\AA})$	$c_0^{expt}(\text{\AA})$	z^{expt}	$E_g(\text{eV})$	$E_g^{expt}(\text{eV})$
MoS ₂	3.179	12.729	0.627	3.160	12.290	0.629	1.060	1.29
MoSe ₂	3.309	13.323	0.624	3.289	12.927	0.621	0.959	1.09
WS ₂	3.183	13.131	0.630	3.150	12.320	0.622	1.283	1.35
WSe ₂	3.319	13.729	0.627	3.282	12.960	0.621	1.188	1.20

TABLE I: Calculated properties of bulk TMDC materials: lattice constant a_0 , c-axis lattice constant c_0 , z-parameter z , and bandgap $E_g(\text{eV})$. Experimental values^{39–41} have been included for comparison.

Structure	Point	MoS ₂	MoSe ₂	WS ₂	WSe ₂	MoS ₂	MoSe ₂	WS ₂	WSe ₂
		Hole Effective Mass (m_0)				Electron Effective Mass (m_0)			
1L	K _l	0.543	0.578	0.339	0.341	0.506	0.502	0.349	0.345
	K _t	0.546	0.588	0.339	0.348	0.504	0.503	0.347	0.345
2L	Γ	1.039	1.430	1.239	1.322	-	-	-	-
	K _l	0.548	0.595	0.345	0.349	0.521	0.539	0.359	0.411
	K _t	0.546	0.596	0.346	0.348	0.510	0.539	0.359	0.412
3L	Γ	1.039	1.432	1.246	1.382	-	-	-	-
	K _t	0.549	0.602	0.366	0.368	0.559	0.544	0.376	0.434
	K _t	0.548	0.604	0.366	0.368	0.559	0.544	0.377	0.434
4L	Γ	1.239	1.433	1.351	1.432	-	-	-	-
	K _l	0.548	0.604	0.366	0.367	0.554	0.542	0.376	0.435
	K _t	0.546	0.604	0.366	0.368	0.559	0.549	0.377	0.434
Bulk	Γ	0.838	0.973	0.832	0.997	-	-	-	-
	Σ_l	-	-	-	-	0.590	0.521	0.569	0.489
	Σ_t	-	-	-	-	0.845	0.776	0.665	0.643

TABLE II: *Ab-initio* calculations of the hole and electron effective masses at the valence band maxima and conduction band minima respectively for each structure in units of the free electron mass (m_0). The subscripts l and t refer to the masses calculated at the symmetry point along the longitudinal and the transverse directions.

Structure	Transition	MoS ₂	MoSe ₂	WS ₂	WSe ₂	MoS ₂	MoSe ₂	WS ₂	WSe ₂
		Calculated (eV)				Experimental (eV)			
1L	K_{v1} to K_c	1.600	1.375	1.548	1.254	1.900	1.660	1.950	1.640
	K_{v2} to K_c	1.750	1.556	1.973	1.715	2.050	1.850	2.360	2.040
	Γ_v to K_c	1.705	1.768	1.849	1.776	-	-	-	-
2L	Γ_v to K_c	1.250	1.186	1.507	1.586	1.600	-	1.730	-
	K_{v1} to K_c	1.600	1.373	1.549	1.269	1.880	-	1.910	1.590
	K_{v2} to K_c	1.760	1.556	1.977	1.788	2.050	-	2.340	2.000
3L	Γ_v to K_c	1.150	1.186	1.458	1.586	-	-	-	-
	K_{v1} to K_c	1.620	1.376	1.549	1.265	-	-	-	-
	K_{v2} to K_c	1.780	1.564	1.937	1.783	-	-	-	-
4L	Γ_v to K_c	1.120	1.046	1.438	1.546	-	-	-	-
	K_{v1} to K_c	1.630	1.356	1.539	1.259	-	-	-	-
	K_{v2} to K_c	1.780	1.574	1.957	1.753	-	-	-	-
Bulk	Γ_v to Σ_c	1.060	0.959	1.283	1.188	1.290	1.090	1.350	1.200
	K_{v1} to K_c	1.590	1.349	1.453	1.258	1.880	1.350	1.880	1.580
	K_{v2} to K_c	1.780	1.588	1.889	1.737	2.060	1.380	2.320	1.950

TABLE III: *Ab-initio* calculations of the bandgap energies and energy transitions between the valence (v) and conduction (c) band valleys for each structure and material. The splitting of the valence band at the K -point due to spin-orbit coupling and the inter-layer interactions are denoted as K_{v1} and K_{v2} . Σ is the mid-point between Γ and K . The bandgap at each dimension is highlighted in bold text. Experimental values when available^{39–41,56} have been included for comparison.

NOTE: The band gap of 2L, 3L and 4L WSe₂ occurs between the K_{v1} and Σ_C . The 2L, 3L and 4L band gaps of WSe₂ are 1.216 eV, 1.1594 eV and 1.1345 eV respectively.

Temperature		1L	2L	3L	4L	Bulk
Maximum n-type (p-type) Power Factor ($WK^{-2}m^{-2}$)						
MoS ₂	300K	.130 (.150)	.140 (.110)	.280 (.041)	.220 (.031)	.0320 (.010)
	150K	.093 (.072)	.093 (.071)	.190 (.032)	.120 (.024)	.012 (.0042)
	77K	.072 (.043)	.072 (.053)	.13 (.021)	.063 (.022)	.012 (.0031)
MoSe ₂	300K	.340 (.071)	.330 (.094)	.230 (.082)	.230 (.071)	.022 (.0061)
	150K	.151 (.050)	.200 (.051)	.100 (.051)	.100 (.052)	.013 (.004)
	77K	.062 (.031)	.120 (.032)	.062 (.031)	.052 (.032)	.013 (.0032)
WS ₂	300K	.240 (.062)	.280 (.061)	.270 (.071)	.240 (.092)	.022 (.0052)
	150K	.110 (.042)	.160 (.042)	.150 (.041)	.130 (.051)	.010 (.0043)
	77K	.051 (.031)	.081 (.032)	.070 (.032)	.081 (.031)	.010 (.0022)
WSe ₂	300K	.260 (.054)	.240 (.052)	.190 (.053)	.160 (.053)	.022 (.014)
	150K	.141 (.030)	.140 (.031)	.081 (.031)	.070 (.031)	.010 (.004)
	77K	.071 (.031)	.082 (.031)	.050 (.031)	.043 (.022)	.011 (0.0021)

TABLE IV: Peak n-type (p-type) power factor of 1L, 2L, 3L, 4L and bulk MoS₂, MoSe₂, WS₂ and WSe₂ at 300K, 150K and 77K. The maximum power factor for each material at a given temperature is in bold.

Temperature		1L	2L	3L	4L	Bulk
Maximum n-type (p-type) ZT						
MoS ₂	300K	1.35 (.970)	1.35 (1.15)	2.23 (.510)	1.78 (.390)	.350 (.081)
	150K	.590 (.350)	.590 (.450)	1.03 (.220)	.660 (.160)	.110 (.034)
	77K	.240 (.140)	.240 (.190)	.420 (.093)	.210 (.062)	.031 (.012)
MoSe ₂	300K	1.39 (.800)	2.39 (.810)	1.66 (.810)	1.65 (.810)	.290 (.081)
	150K	.450 (.310)	1.06 (.320)	.610 (.320)	.570 (.320)	.100 (.033)
	77K	.130 (.120)	.410 (.120)	.220 (.120)	.170 (.120)	.030 (.014)
WS ₂	300K	1.52 (.70)	1.98 (.720)	2.03 (.760)	1.85 (.760)	.280 (.082)
	150K	.411 (.280)	.613 (.280)	.770 (.280)	.721 (.350)	.104 (.030)
	77K	.120 (.110)	.181 (.113)	.211 (.113)	.271 (.113)	.034 (.012)
WSe ₂	300K	1.88 (.620)	1.92 (.620)	1.44 (.620)	1.13 (.620)	.260 (.120)
	150K	.590 (.220)	.750 (.220)	.490 (.220)	.380 (.220)	.091 (.032)
	77K	.180 (.100)	.270 (.100)	.170 (.100)	.130 (.100)	.031 (.014)

TABLE V: Peak n-type (p-type) thermoelectric figure of merit, ZT, of 1L, 2L, 3L, 4L and bulk MoS₂, MoSe₂, WS₂ and WSe₂ at 300K, 150K and 77K. The maximum ZT for each material at a given temperature is in bold.